Heart-rate sensitive optical coherence angiography for measuring vascular changes due to posttraumatic brain injury in mice

Jordi L. Tremoleda
Karl Alvarez
Abdirahman Aden
Robert Donnan
Adina T. Michael-Titus
Peter H. Tomlins

SPIE.

Heart-rate sensitive optical coherence angiography for measuring vascular changes due to posttraumatic brain injury in mice

Jordi L. Tremoleda,[a] Karl Alvarez,[b] Abdirahman Aden,[c] Robert Donnan,[b] Adina T. Michael-Titus,[a] and Peter H. Tomlins[c,*]
[a]Queen Mary University of London, Blizard Institute, Barts and the London School of Medicine and Dentistry, Centre for Trauma Sciences, London, United Kingdom
[b]Queen Mary University of London, School of Electrical Engineering and Computer Science, London, United Kingdom
[c]Queen Mary University of London, Institute of Dentistry, Barts and the London School of Medicine and Dentistry, London, United Kingdom

Abstract. Traumatic brain injury (TBI) results in direct vascular disruption, triggering edema, and reduction in cerebral blood flow. Therefore, understanding the pathophysiology of brain microcirculation following TBI is important for the development of effective therapies. Optical coherence angiography (OCA) is a promising tool for evaluating TBI in rodent models. We develop an approach to OCA that uses the heart-rate frequency to discriminate between static tissue and vasculature. This method operates on intensity data and is therefore not phase sensitive. Furthermore, it does not require spatial overlap of voxels and thus can be applied to pre-existing datasets for which oversampling may not have been explicitly considered. Heart-rate sensitive OCA was developed for dynamic assessment of mouse microvasculature post-TBI. Results show changes occurring at 5-min intervals within the first 50 min of injury. © *The Authors. Published by SPIE under a Creative Commons Attribution 3.0 Unported License. Distribution or reproduction of this work in whole or in part requires full attribution of the original publication, including its DOI.* [DOI: 10.1117/1.JBO.22.12.121710]

Keywords: optical coherence angiography; microvasculature; traumatic brain injury.

Paper 170501SSLRR received Jul. 31, 2017; accepted for publication Nov. 9, 2017; published online Dec. 5, 2017.

1 Introduction

Traumatic brain injury (TBI) is a major cause of morbidity and disability.[1] Primary injury triggers a secondary cascade of inflammatory and neurometabolic progressive events[2] that lead to neuronal loss and diffuse axonal injury, associated with the functional deficits detected in TBI patients.[3] Furthermore, TBI leads to an increasing risk of developing long-term neurodegenerative conditions.[4] Unfortunately, to date there are no effective treatments to counter such acute or chronic events.

One of the key pathological events that occurs at the onset of TBI is direct vascular disruption. This triggers subsequent edema and reduction in cerebral blood flow, which leads to axonal degeneration and cell death.[5] Until recently, it was difficult to observe these effects *in vivo*. However, advances in reflection optical imaging have facilitated intraoperative imaging of cerebral microcirculation on the brain surface.[6] However, such two-dimensional methods are unable to discriminate planes within a three-dimensional (3-D) volume. Real-time 3-D imaging in tissue can be achieved using optical coherence tomography (OCT)[7,8] and vasculature can be differentiated from static tissue using a variety of processing algorithms, collectively called optical coherence angiography (OCA),[9] which has been applied specifically to neuroscience[10] and ophthalmology.[11,12] OCA algorithms can be broadly divided into phase and intensity methods. Phase-based methods derive from Doppler OCT,[13] whereby light scattered from flowing red blood cells introduces

a Doppler shift that is detected as a phase shift in the OCT signal. Intensity-based methods rely upon detecting statistical differences in light scattered from flowing and static tissue. For example, correlation mapping[14,15] assumes that blood flow reduces the temporal correlation between sequential *B*-scans. Speckle variance techniques exploit the temporal intensity variations of speckle to discriminate microvasculature.[16–18] Optical microangiography[19,20] utilizes both phase and amplitude variations.

Photoplethysmography (PPG)[21] is an established clinical technique used to measure blood volume changes in skin microvasculature. A single photodetector measures a heart-beat-modulated change in scattered light intensity that occurs when the heart beat affects an increase or decrease in local red blood cell density. OCT measures spatially resolved backscattered light and therefore each OCT pixel should be able to act as a PPG detector. In this case, the heart-beat is a natural, rather than artificial[22,23] carrier frequency that facilitates discrimination between vasculature and static tissue.

Therefore, the aim of this research was to determine whether the natural pulse could be used to isolate microvasculature from static tissue and thus to visualize brain–blood volume dynamics post-TBI using OCT data.

2 Theory

The periodic systole and diastole of the heart muscle yields a pulsed flow of blood around the cardiovascular system. During systole, the density of blood cells within the vessels increases. Similarly, diastolic pressure results in a relative decrease in blood cell density. Consequently, there is a

*Address all correspondence to: Peter H. Tomlins, E-mail: p.h.tomlins@qmul.ac.uk

corresponding change in the local optical scattering properties of the blood. OCT images represent a spatial map of backscattered light intensity. Therefore, each pixel or voxel in an OCT image represents the intensity of light detected from its corresponding location within the sample.

Suppose that a living tissue is imaged with OCT in a 3-D Cartesian coordinate system defined by two lateral dimensions (x, y) and an axial dimension z. The detected backscattered light intensity from any spatiotemporal point $I_{x,y,z}(t)$ can be expressed [Eq. (1)] as the sum of a static component $S_{x,y,z}$ and a time-dependent component due to vascular blood flow $V_{x,y,z}(t)$, where t represents time

$$I_{x,y,z} = S_{x,y,z} + V_{x,y,z}(t). \tag{1}$$

Within blood vessels, the heart-beat modulates the backscattered light intensity at a frequency f_h with amplitude $A_{x,y,z}$ such that

$$V_{x,y,z}(t) = A_{x,y,z} \sin(2\pi f_h t). \tag{2}$$

Thus, by monitoring $I_{x,y,z}(t)$ over time, blood vessels are identified by the presence of intensity modulation at frequency f_h. Fourier transformation of $I_{x,y,z}(t)$ decomposes the signal into frequency components located at DC and $\pm f_h$ corresponding to static tissue and vascular flow, respectively. Therefore, if the heart-beat frequency is known, it can be isolated to separate vascular and static tissue.

According to the Nyquist–Shannon sampling theory, the minimum sampling rate is $f_{\min} > 2 f_h$. In sedated mouse models, the heart rate is expected in the range $5 < f_h < 10$ Hz (300 to 600 bpm).[24,25] Thus, the minimum sampling rate required is $f_{\min} = 20$ Hz. In spectral-domain OCT, each axial scan (A-scan) is acquired by a single spectrometer exposure at a rate $f_{A\text{scan}}$. Raster-scanning acquisition yields a corresponding B-scan rate, $f_{B\text{scan}} = f_{A\text{scan}}/P$, where P is the number of A-scans per B-scan (x, z plane—see Fig. 1). Setting $f_{B\text{scan}} = f_{\min}$, then $f_{A\text{scan}} \geq P f_{\min}$. For an OCT B-scan comprising $P = 500$ A-scans, the A-scan rate required to sample mouse vasculature is, therefore, $f_{A\text{scan}} \geq 10$ kHz.
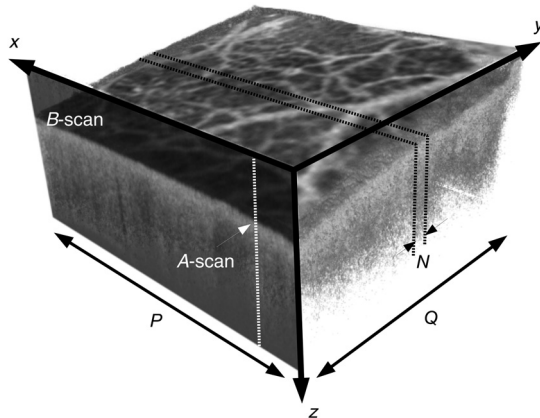
3 Materials and Methods

The spectral-OCT system used for this study incorporated a fiber optic interferometer and superluminescent light emitting diode (SLD1325, Thorlabs, Cambridge, United Kingdom), operating at a central wavelength of 1325 nm over a bandwidth of >100 nm. The spectrometer consists of an InGaAs linear detector array (SU-LDH2, Sensors Unlimited), a reflective diffraction grating and focusing/collimating achromatic doublet lenses (75-mm focal length). Images were obtained by raster scanning the probe beam over the tissue surface using a 2-D galvanometer configuration (GVS012, Thorlabs, United Kingdom).

3-D OCT volumes were $500 \times 500 \times 512$ pixels (x, y, z) acquired over an *en face* area measuring 3.5×3.5 mm. Vasculature mapping was postprocessed offline using MATLAB® (MATLAB R2014b, The MathWorks Inc.) as described below.

According to the geometry shown in Fig. 1, vasculature maps were obtained from the B-scan intensity image volumes. For each (x, z) coordinate within the volume, the adjacent $N = 16$ voxels along the y-direction were selected, i.e., $I_{\text{sub}} = \{I_{x,y,z}, I_{x,y+1,z}, \ldots, I_{x,y+N-1,z}\}$ as shown in Fig. 2. A Blackman window of length $N = 16$ was applied to I_{sub} along y to suppress edge effects. I_{sub} was zero padded to a length of 32 elements for minor improvements in vascular discrimination. Positive frequency components of I_{sub} were determined from the absolute magnitude of its one-dimensional fast fourier transform (FFT). The upper quarter of the frequency spectrum corresponded to the expected heart-rate range. Thus, its total sum was taken to represent the contribution of blood flow within I_{sub}. This process was repeated throughout the image volume to produce a new volume, I_{OCA}, in which the intensity represented the strength of high-frequency components, the strongest of which originated within blood vessels due to the heart-beat modulation. Signal strength was enhanced by elementwise multiplication of I_{OCA} with the original OCT image data. Consequently, regions of strong OCT signal were given a higher weighting than those containing noise. For ease of visualization, 2-D vasculature projections were produced as a standard deviation map along the axial z-axis.

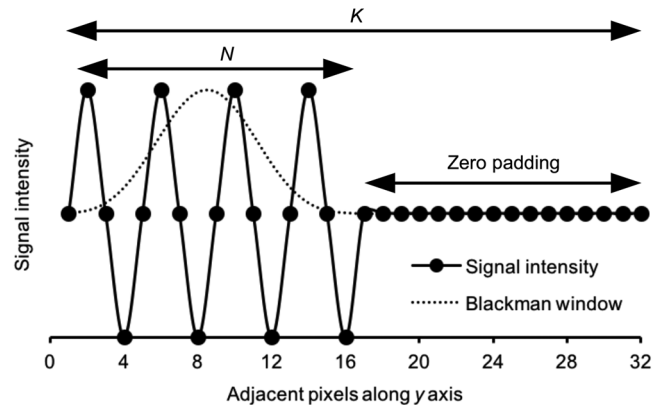Adult 12 to 14-week-old C57BL/6 mice, with a nominal weight of 33 g (Charles River Laboratories, Harlow, United

Fig. 1 OCT image volume and associated coordinate system. Each B-scan consists of P A-scans, acquired sequentially along the x-direction. An OCT volume consists of Q B-scan images acquired along the y-direction. Pixels along the y-direction from N adjacent B-scans were used to determine the frequency components.

Fig. 2 Signal intensity, I_{sub}, for pixels along the y-axis from $N = 16$ adjacent B-scans, zero padded to a total length of 32. The modulated signal, due to a heart rate of 300 bpm (5 Hz), was windowed by a Blackman function.

Kingdom), were used. Mice were housed in standard cages in a 12-h light/dark cycle and given specific diet and water *ad libitum*. All animal procedures were approved by the Animal Welfare and Ethical Review Body at Queen Mary University of London, and the UK Home Office, in accordance with the EU Directive 2010/63/EU. A controlled cortical impact (CCI) TBI model was used in this study.[26] Briefly, after a 1-week acclimatization period, the mice were anesthetized using a mixture of ketamine (50 mg/kg) and medetomidine (0.5 mg/kg) in sterile saline, administered intraperitoneally (i.p.). Once anaesthetized, fur was shaved over the dorsal head area, and animals were placed in a stereotaxic frame. A midline longitudinal incision was performed to expose the skull. Two 3-mm craniotomies (right and left parietal bone) were carried out using a pneumatic fine-drill, 2.0 mm away from bregma and 2.5-mm lateral, at either side of the midline. A controlled impaction injury was induced using the PCI3000 Precision Cortical Impactor™ (Hatteras Instruments, Inc.), with an impactor tip of 3 mm and using an impact speed of 3 m/s, a depth of 2.2 mm, and a dwell time of 100 ms. Animals were maintained in the stereotaxic frame following injury to carry out the imaging acquisitions through both craniotomy windows, in the injury site in the right hemisphere and in the left noninjured hemisphere. Sterile saline was instilled in the exposed area to avoid tissue desiccation, and a temperature-controlled warming pad was used to monitor and maintain the animal core-body temperature (∼37°C), throughout the whole procedure.

The OCT imaging probe was attached two 300-mm travel linear translation stages (LTS300, Thorlabs Ltd., United Kingdom) mounted in a vertical and horizontal configuration, as shown in Figs. 3(a)–3(c). The translation stages were operated under computer control. A pre-TBI image was obtained through both the left (control) and right (TBI) craniotomy windows of the same animal, using the linear translation stages to control and record the positions. To administer TBI, the probe was moved away from the mouse [Fig. 3(a)]. Within 30 s of TBI, the translation stages repositioned the probe and acquired OCT image volumes through the right [Fig. 3(b)] and left [Fig. 3(c)] craniotomy windows. Imaging of the brain through the left and right craniotomy windows continued at 5-min intervals for duration of 50 min post-TBI.
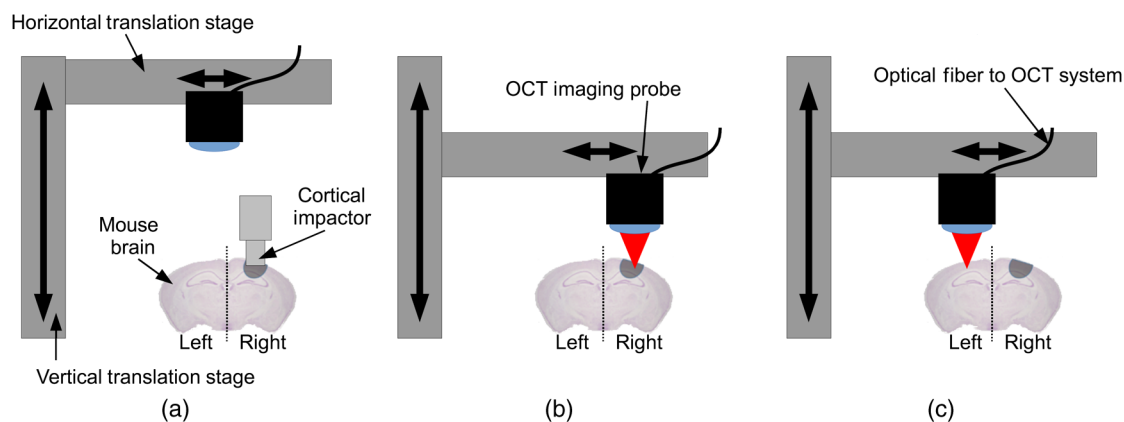
4 Results and Discussion

OCA images for Fourier components $0.0 \leq f < 2.5$ Hz, $2.5 \leq f < 5.0$ Hz, $5.0 \leq f < 7.5$ Hz, and $7.5 \leq f < 10.0$ Hz are shown in Figs. 4(a)–4(d). For comparison, the images are presented on a logarithmic intensity scale over a 10-dB dynamic range from the static tissue noise floor.

No vasculature was evident at $f < 5.0$ Hz [Figs. 4(a)–4(b)]. Low-contrast vasculature was visible in Fig. 4(c), corresponding ($5.0 \leq f < 7.5$ Hz). However, the clearest vasculature signal corresponded with the expected heart-beat frequency range, $7.5 \leq f < 10$ Hz [Fig. 4(d)]. Consequently, the highest frequency quadrant was used for vascular imaging.

OCA image projections for one of the specimens are shown in Fig. 5. The vascular distribution pre-TBI can be visually compared with post-TBI OCA projections at 5-min intervals following TBI. Projections are shown up to 15 min post-TBI, with a reduction in the visible vasculature within the region of TBI. The circular outline of the cortical impactor can also be observed within the images.

This work was conducted using a CCI TBI model.[27] This model uses a 3-mm-diameter impactor tip to induce a focal cortical injury directly onto the exposed brain cortex. The speed (3 m/s), depth (2.2 mm), and dwell time (100 ms) were all standardized to produce an injury of "moderate" severity. This classification is based on histopathological and behavioral outcomes that have been well investigated in similar models and shown to provide experimental reliability and reproducibility.[28] A feature of the CCI-TBI model used in this study is that it was necessary to open the skull prior to inducing TBI; however, Fig. 4 shows that cortical vasculature was obtained from the OCT data prior to craniotomy (and TBI) through the intact skull.

This highlights one of the advantages of OCT-based angiography methods over 2-D reflection imaging techniques. OCT-based methods work implicitly with 3-D image volumes. Therefore, vasculature can be discriminated in different planes. For example, Fig. 4 was acquired through the intact skull. Vasculature that is present within the skull was rejected by forming the projection images from below the skull depth. This demonstrates how 3-D regions of interest can be selected for examination. In this work, the 3-D data were rendered as 2-D projections. However, the underlying datasets remain 3-D. In

Fig. 3 The OCT imaging probe was mounted on a vertical and horizontal translation stages for positional control of mouse brain imaging. (a) The probe was moved away to allow the use of a cortical impactor to administer a primary insult to the right hemisphere. Following TBI, the imaging probe was moved into its *a priori* determined imaging positions to acquire OCT volumes of the (b) right and (c) left brain hemispheres.
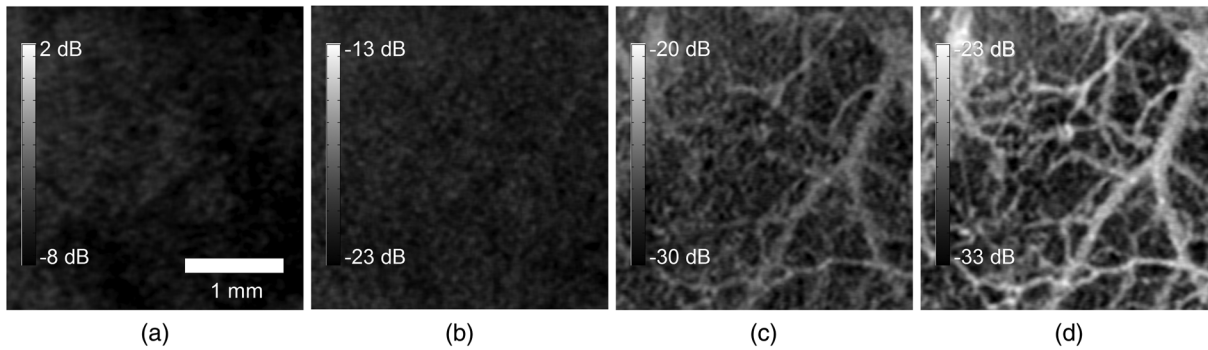
Fig. 4 OCT standard deviation projections of different Fourier components f, (a) $0.0 \leq f < 2.5$ Hz, (b) $2.5 \leq f < 5.0$ Hz, (c) $5.0 \leq f < 7.5$ Hz, and (d) $7.5 \leq f < 10$ Hz. These images were obtained through the intact, exposed mouse skull prior to TBI. In each case, the logarithmic intensity scale is over a 10-dB dynamic range above the static tissue noise floor.
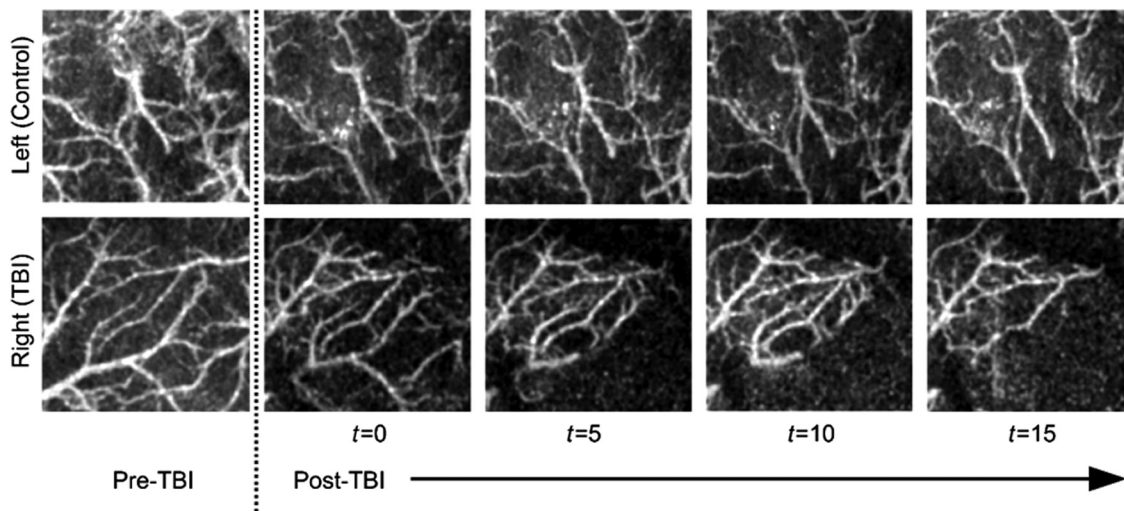

Fig. 5 Comparison of left and right sides of a mouse brain, pre- and post-TBI, where the TBI was administered to the right hemisphere. The post-TBI images were acquired at 5-min intervals, $t = 0$, 5, 10, and 15 min. Measurements were made up to 50 min post-TBI.

TBI, this is important because tissue disruption can impair anatomical understanding and interpretation of 2-D reflection images.

The animals were anesthetized throughout the study, which may have introduced some hemodynamic effects. However, in this work ketamine was used, which is being increasingly applied as an alternative sedative in the acute management of TBI patients. It has recently been reported that ketamine is not associated with an increased risk of modification of intracranial pressure and may confer neuroprotective effects in patients at risk of ischemic brain injury, thus reducing cell death and neuronal degeneration.[29]

The primary question addressed by this work was whether the heart rate can be used as a natural modulation frequency to discriminate perfused vasculature from surrounding tissue in volumetric OCT data. Figure 4 shows four different frequency components of the same region of mouse brain imaged through the intact skull. All images were displayed on the same intensity scale, showing a high signal contribution from DC and low frequencies. These are explained by static tissue and motion, such as breathing. Higher frequencies contain the vasculature that is dominated by heart-beat modulation. There is some

spread in the detected frequencies, which may come from the heart-beat signal departing from a pure sine wave, containing multiple frequency components, which could be used to investigate the heart beat pulse shape. Similar characteristics have been previously reported in PPG studies.[30]

Potential OCT sensitivity to heart frequency components and pulse shape are important for understanding the pathophysiological changes associated with TBI. This is because TBI injury induces a systemic catecholamine "storm" driven by the central neuroendocrine axis and cortical damage induces dysfunction of the autonomic nervous systems and an intense inflammatory response, all of which have major adverse effects on the heart.

Nevertheless, the fundamental theoretical principle appears to be supported, with the results showing that the natural heart-rate modulation can be used to discern static tissue from blood flow in OCT data.

There are a few advantages over other OCA techniques. The rejection of noise is based upon detecting the physical process responsible for blood flow rather than relying purely upon statistical differences between tissues. Furthermore, no oversampling or interferometric phase information is required. Although a comparison with other methods is beyond the scope of this

paper, this work was partially motivated by the requirement to measure dynamic vasculature events. While other techniques have shown promising results, these can be at the expense of acquisition speed. Furthermore, the method presented here is not mutually exclusive and can be applied in conjunction with other methods to enhance signal.

The focus of this work was dynamic neuroimaging in mice. However, assuming a resting human heart rate $1 < f_h < 2$ Hz (60 to 120 bpm), the required A-scan rate for imaging human microvasculature is $f_{Ascan} = 2$ kHz. Thus, it is feasible to apply this technique to human microvasculature imaging, opening new avenues for imaging microvasculature in real-time with a high temporal resolution.

Clinically, it may be possible to directly visualize vascular supply to the cortical area during intrasurgical interventions in which a craniotomy is applied. However, imaging through the human skull remains a challenge for OCT-based neuroimaging. Nevertheless, the presented method of vascular imaging offers advances to the study of inflammation and wound-healing in clinical fields, such as dermatology and periodontology, where tissue is directly accessible. For example, periodontitis (gum disease) affects a large percentage of the population,[31] being ranked as the sixth most prevalent human disease globally.[32] Studying the vasculature of inflamed periodontal tissue is important because it is associated with chronic infections, tooth loss, and various systemic complications, such as diabetes, cardiovascular disease, and rheumatoid arthritis.[33–36] Furthermore, in oral surgery, tissue healing is not well understood.

Time-resolved neuroimaging in preclinical TBI models is extremely valuable, being essential for the development and translation of treatments. This work has focused on discriminating vasculature from static tissue. However, future Fourier analysis of the modulated OCT signal should build upon previous PPG studies[30,37] to investigate changes to the heart pulse shape in response to TBI and potential protective therapies.

Disclosures

The authors have no relevant financial interests in this article and no potential conflicts of interest to disclose.

Acknowledgments

References

1. T. Roebuck-Spencer and A. Cernich, "Epidemiology and societal impact of traumatic brain injury," in *Handbook on the Neuropsychology of Traumatic Brain Injury*, M. Sherer and A. M. Sander, Eds., pp. 3–23, Springer, New York (2014).
2. Z. M. Weil, K. R. Gaier, and K. Karelina, "Injury timing alters metabolic, inflammatory and functional outcomes following repeated mild traumatic brain injury," *Neurobiol. Dis.* **70**, 108–116 (2014).
3. V. E. Johnson, W. Stewart, and D. H. Smith, "Axonal pathology in traumatic brain injury," *Exp. Neurol.* **246**, 35–43 (2013).
4. N. Pearce, V. Gallo, and D. McElvenny, "Head trauma in sport and neurodegenerative disease: an issue whose time has come?" *Neurobiol. Aging* **36**(3), 1383–1389 (2015).
5. C. Betrus and C. W. Kreipke, "Historical perspectives in understanding traumatic brain injury and in situating disruption in CBF in the pathotrajectory of head trauma," in *Cerebral Blood Flow, Metabolism, and Head Trauma*, C. W. Kreipke and J. A. Rafols, Eds., pp. 1–27, Springer, New York (2013).
6. J. Pérez-Bárcena et al., "Direct observation during surgery shows preservation of cerebral microcirculation in patients with traumatic brain injury," *J. Neurol. Sci.* **353**(1–2), 38–43 (2015).
7. P. H. Tomlins and R. K. Wang, "Theory, developments and applications of optical coherence tomography," *J. Phys. Appl. Phys.* **38**, 2519–2535 (2005).
8. L. I. Kramoreva and Y. I. Rozhko, "Optical coherence tomography (review)," *J. Appl. Spectrosc.* **77**(4), 449–467 (2010).
9. A. Zhang et al., "Methods and algorithms for optical coherence tomography-based angiography: a review and comparison," *J. Biomed. Opt.* **20**(10), 100901 (2015).
10. U. Baran and R. K. Wang, "Review of optical coherence tomography based angiography in neuroscience," *Neurophotonics* **3**(1), 010902 (2016).
11. T. E. de Carlo et al., "A review of optical coherence tomography angiography (OCTA)," *Int. J. Retina Vitr.* **1**, 5 (2015).
12. A. Wylęgała et al., "Optical coherence angiography: a review," *Medicine* **95**(41), e4907 (2016).
13. Z. Chen et al., "Optical Doppler tomographic imaging of fluid flow velocity in highly scattering media," *Opt. Lett.* **22**, 64–66 (1997).
14. E. Jonathan, J. Enfield, and M. J. Leahy, "Correlation mapping method for generating microcirculation morphology from optical coherence tomography (OCT) intensity images," *J. Biophotonics* **4**(9), 583–587 (2011).
15. J. Enfield, E. Jonathan, and M. Leahy, "In vivo imaging of the microcirculation of the volar forearm using correlation mapping optical coherence tomography (cmOCT)," *Biomed. Opt. Express* **2**(5), 1184–1193 (2011).
16. J. K. Barton and S. Stromski, "Flow measurement without phase information in optical coherence tomography images," *Opt. Express* **13**(14), 5234–5239 (2005).
17. A. Mariampillai et al., "Optimized speckle variance OCT imaging of microvasculature," *Opt. Lett.* **35**(8), 1257–1259 (2010).
18. C. Blatter et al., "Ultrahigh-speed non-invasive widefield angiography," *J. Biomed. Opt.* **17**(7), 070505 (2012).
19. L. An, J. Qin, and R. K. Wang, "Ultrahigh sensitive optical microangiography for in vivo imaging of microcirculations within human skin tissue beds," *Opt. Express* **18**(8), 8220–8228 (2010).
20. R. K. Wang et al., "Depth-resolved imaging of capillary networks in retina and choroid using ultrahigh sensitive optical microangiography," *Opt. Lett.* **35**(9), 1467–1469 (2010).
21. H. Rajaguru and S. K. Prabhakar, "A comprehensive review on photoplethysmography and its application for heart rate turbulence clinical diagnosis," *Adv. Sci. Lett.* **21**(12), 3602–3604 (2015).
22. R. K. Wang, "Three-dimensional optical micro-angiography maps directional blood perfusion deep within microcirculation tissue beds in vivo," *Phys. Med. Biol.* **52**(23), N531–N531 (2007).
23. R. K. Wang, "Directional blood flow imaging in volumetric optical microangiography achieved by digital frequency modulation," *Opt. Lett.* **33**(16), 1878–1880 (2008).
24. A. Tsukamoto et al., "Vital signs monitoring during injectable and inhalant anesthesia in mice," *Exp. Anim.* **64**(1), 57–64 (2015).
25. C. Constantinides, R. Mean, and B. J. Janssen, "Effects of isoflurane anesthesia on the cardiovascular function of the C57BL/6 mouse," *ILAR J.* **52**, e21–e31 (2011).
26. N. D. Osier, J. R. Korpon, and C. E. Dixon, "Controlled cortical impact model," Chapter 16 in *Brain Neurotrauma: Molecular, Neuropsychological, and Rehabilitation Aspects*, F. H. Kobeissy, Ed., CRC Press/Taylor and Francis, Boca Raton, Florida (2015).
27. G. B. Fox et al., "Sustained sensory/motor and cognitive deficits with neuronal apoptosis following controlled cortical impact brain injury in the mouse," *J. Neurotrauma* **15**(8), 599–614 (1998).
28. Y. Xiong, A. Mahmood, and M. Chopp, "Animal models of traumatic brain injury," *Nat. Rev. Neurosci.* **14**(2), 128–142 (2013).
29. M. Oddo et al., "Optimizing sedation in patients with acute brain injury," *Crit. Care* **20**, 128 (2016).
30. M. Elgendi, "On the analysis of fingertip photoplethysmogram signals," *Curr. Cardiol. Rev.* **8**(1), 14–25 (2012).
31. B. L. Pihlstrom, B. S. Michalowicz, and N. W. Johnson, "Periodontal diseases," *Lancet* **366**(9499), 1809–1820 (2005).
32. W. Marcenes et al., "Global burden of oral conditions in 1990–2010: a systematic analysis," *J. Dent. Res.* **92**(7), 592–597 (2013).

33. P. M. Preshaw et al., "Periodontitis and diabetes: a two-way relationship," *Diabetologia* **55**(1), 21–31 (2012).

34. L. Nibali et al., "Association between metabolic syndrome and periodontitis: a systematic review and meta-analysis," *J. Clin. Endocrinol. Metab.* **98**(3), 913–920 (2013).

35. A. A. Bahekar et al., "The prevalence and incidence of coronary heart disease is significantly increased in periodontitis: a meta-analysis," *Am. Heart J.* **154**(5), 830–837 (2007).

36. J. B. Payne et al., "The link between periodontitis and rheumatoid arthritis: a periodontist's perspective," *Curr. Oral Health Rep.* **2**(1), 20–29 (2015).

37. A. L. Rivera et al., "Loss of breathing modulation of heart rate variability in patients with recent and long standing diabetes mellitus type II," *PLoS One* **11**(11), e0165904 (2016).

Biographies for the authors are not available.